Date of publication xxxx xx, xxxx, date of current version February 18, 2026.

Digital Object Identifier 10.xxxx/ACCESS.2026.xxxxxxx

Beamforming Optimization and System Level Assessment in RIS-Aided MIMO Systems Comprising Hybrid Precoding Architectures

DIOGO MENDES[1,2], (Graduate Student Member, IEEE), JOÃO PEDRO PAVIA[3,4], (Member, IEEE), NUNO SOUTO[1,2], (Senior Member, IEEE), JOÃO SILVA[1,4], and AMÉRICO CORREIA[1,2], (Senior Member, IEEE)

[1]Department of Information Science and Technology, Iscte - Instituto Universitário de Lisboa, 1649-026 Lisboa, Portugal
[2]Instituto de Telecomunicações (IT), 1049-001 Lisboa, Portugal
[3]Department of Applied Digital Technologies, Iscte - Instituto Universitário de Lisboa, 2710-569 Sintra, Portugal
[4]Information Sciences and Technologies and Architecture Research Centre (ISTAR), 1649-026 Lisboa, Portugal

Corresponding author: Diogo Mendes (e-mail: Diogo_Roque@iscte-iul.pt).

This work was partially supported by Instituto de Telecomunicações, Lisboa, Portugal and FCT/MCTES through national funds and when applicable co-funded EU funds under the project UIDB/50008/2020 and UIDB/04466/2025. Moreover, this work was also partially supported by ISTAR and FCT/MCTES under the projects UIDB/04466/2020 and UIDP/04466/2020.

ABSTRACT The terahertz (THz) band is a candidate technology for future sixth-generation (6G) wireless networks that could support increasingly demanding requirements, such as high wireless traffic volumes and transmission rates. However, the limited range and high propagation losses at these frequencies present several challenges that must be overcome. One emerging solution is the use of reconfigurable intelligent surfaces (RIS), which optimize communication network performance in combination with ultra-massive multiple-input multiple-output (UM-MIMO) antennas. UM-MIMO's large number of antennas provides highly directional beams, enabling reliable data propagation from the transmitter to the receiver at THz frequencies. However, it can substantially increase implementation complexity. This paper proposes a joint hybrid precoder and RIS optimization algorithm to overcome these challenges. The algorithm is designed to maximize the achievable rate of THz UM-MIMO communications by segregating digital and analog precoder computations and adopting hybrid architectures: fully connected (FC), array-of-subarrays (AoSA), and dynamic array-of-subarrays (DAoSA). The proposed algorithm supports multicarrier transmission and the use of multiple, parallel RIS panels deployed throughout the propagation path. Numerical simulations demonstrate the efficiency and versatility of the algorithm, particularly in contexts where THz systems operate under severe constraints. System-level simulations in a 300 GHz office environment reveal that distributing multiple parallel RIS panels throughout the environment yields the maximum achievable throughput. RIS deployment offers the greatest coverage and throughput gains in low-density scenarios but provides diminishing returns as density increases.

INDEX TERMS 6G, Hybrid Precoding, RIS, THz communications, UM-MIMO

I. INTRODUCTION

RECENT years have been marked by an unprecedented growth in the number of devices interconnected across wireless communication networks. Along with this phenomenon and to cope with the challenges of connectivity, low latency, and high bit rates, an evolution of wireless communication systems is increasingly required in support of this paradigm shift [1].

The development of 6G communication systems emerged in response to the limitations of current Long Term Evolution (LTE) and fifth-generation (5G) systems. According to ITU-R Recommendation M.2083, 5G is designed to achieve a downlink data rate of up to 20 gigabits per second (Gbps) [2], [3]. As a result, the increasing pace of wireless communications worldwide means that 5G communications are no longer sufficient. The volume of data is growing, as are the binary throughput requirements. This compromises the user-level experience, which was one of 5G's greatest strengths. The transition from 5G to 6G requires improving energy and spectrum efficiency to allow the peak data rate to increase

from the current theoretical maximum of 20 gigabits per second (Gbps) to 1 terabit per second (Tbps) [4].

Millimeter wave (mmWave) bands (30-300 GHz) are being adopted to support 5G technologies. Additionally, this band will be crucial for the deployment of 6G technologies, enabling indoor wireless communications systems to reach gigabit-per-second data rates. The mmWave spectrum is divided into multiple smaller frequency blocks, each of which may have a different bandwidth depending on the user's requirements for the proposed 5G service. In particular, the 28 GHz band has been successfully developed and deployed for commercial use in several countries, including Japan and the United States [5].

The terahertz (THz) band is considered a key wireless technology for meeting the future requirements of 6G systems and solving the spectrum scarcity problem observed in mmWave systems due to reduced bandwidth availability [1], [6]. The large bandwidth available in the THz band enables transmission of high data rates of up to Tbps. This provides higher spectrum efficiency, faster speeds, and lower latency compared to existing millimeter wave (mmWave) systems [7].

Although THz waves allow for higher data rates over the wireless network, their range is limited because of the very short wavelengths, which are more susceptible to atmospheric propagation loss that affects the entire communication channel. This creates spectral windows with different bandwidths and distance variations, resulting in high path attenuation for line-of-sight (LoS) links [1]. Furthermore, the THz channel is highly sparse when electromagnetic waves are reflected, refracted, or absorbed by rough surfaces. This results in attenuation and waves scattered in all directions. The higher the frequency used, the greater the degree of sparsity [8]. The THz band severely limits feasible transmitter-to-receiver distances, requiring the implementation of high-gain antennas capable of directing the incoming signal for it to be successfully transmitted.

Multiple-input multiple-output (MIMO) is a fundamental key technology for wireless communication systems, as it utilizes multiple antennas at both ends of the link to increase the spectral efficiency, the spatial degree of freedom (DoF), as well as the number of users that can be served simultaneously. In addition, such systems are capable of handling multiple streams of data, as described in [9], [10]. To overcome the high path loss and interference observed in both mmWave and THz bands, high-gain antennas are employed in MIMO systems. In fact, given the increasing demands of these bands, UM-MIMO becomes essential, as these systems allow the large number of antenna elements present at each end to be grouped, thereby increasing the transmission throughput and steering the narrow beam onto the strongest possible path between the transmitter and receiver [9]. By implementing beamforming in massive MIMO systems, it is possible to increase spectrum efficiency and also multipath capability, overcoming the attenuation present in mmWave and THz frequency bands, thus increasing the communication distance.

RISs, due to their programmable capability to alter the properties of the incident EM wave and direct it to the desired user without the need for power amplifiers or sophisticated signal processing, have attracted the attention of the scientific community and industry as a promising technology for THz systems [11], [12]. Such a capability is especially important for the creation of intelligent wireless communication environments, namely Smart Radio Environments (SRE), which can help overcome the severe limitation of signal transmission distance in the THz band, as described in [13], [14]. Because propagation at high carrier frequencies suffers greatly from blockage between the transmitter and receiver, the reliability of the LoS path is limited. Therefore, it is necessary to create multiple possible paths (multi-paths) to ensure unrestricted coverage when the LoS is obstructed. Thus, MIMO systems aided by RIS panels implemented on metamaterials or metasurfaces can be expected to be a good solution to improve the propagation paths that are severely degraded in the THz band, overcoming the high energy absorption that occurs during communication from the transmitter antennas to the receiver using the THz frequency band.

The implementation of RIS panels in communication systems has been evaluated in [14] and [15], where the authors propose a physical channel modeling for RIS-aided wireless communication systems in the mmWave band. The introduction of RIS structures for the THz band is based on a RIS graphene model, where this framework is considered as one of the most efficient structures towards the THz frequency spectrum for almost completely reflecting the THz wave in an operating frequency range of 0.1 to 4 THz [16]. Some optimization/beamforming designs for RIS-based MIMO communication systems in the mmWave and THz frequency bands have already been explored in [17]–[26]. In particular, in [20], [25], [26] the authors have developed optimization frameworks that maximize the system's capacity and achievable rate while aiming to minimize outage probability and transmit power. Furthermore, the authors in [26] consider a mobile mmWave MIMO system, and propose a blockage-aware, outage-constrained beamforming framework to minimize outage probability and maximize achievable rate simultaneously. These works have demonstrated that the joint optimization of the precoding structure and RIS elements leads to enhanced spectral and energy efficiency, and a better bit error rate (BER) performance, resulting in an improved MIMO wireless communication design in the mmWave/THz frequency bands, which can become a viable solution to achieve 6G performance requirements.

Deploying multiple RIS panels in UM-MIMO environments introduces significant technical challenges beyond those encountered with single-RIS setups. First, the algorithmic and computational complexity increases considerably because jointly optimizing the BS precoders and the phase shifts of several RIS panels creates high-dimensional, non-convex problems. Often, these problems require techniques such as alternating optimization or semidefinite relaxation, which are not always scalable or practical for large systems [27], [28].

Furthermore, although link-level assessment is necessary to evaluate local rate gains, only a system-level evaluation can realistically capture broader performance trends in coverage, user interference, and multi-cell coordination. This approach is especially relevant in scenarios with distributed RIS deployments or coordinated RAN architectures, where metrics such as average throughput, edge coverage, and network-wide capacity are critical for understanding deployment viability. Studies in the literature, such as [19], [21], [23], [29], [30], demonstrate that using multiple RIS panels can overcome severe signal blockage between the base station and users. This allows the system to achieve improved rates, service throughput, and coverage. Furthermore, multiple RISs can enhance the rank of the MIMO channel matrix, mitigate multipath fading, and optimize the performance of spatial multiplexing by adjusting the RIS-assisted communication channel. This is particularly important in multi-stream and multi-carrier systems, where establishing multiple strong propagation paths is desirable yet challenging to accomplish in the THz band due to channel sparsity. Regarding the practicality of RIS implementation in THz band systems, recent literature (e.g., [31]) has shown promising results, demonstrating that RISs can effectively enhance communications system capabilities.

Although RISs have been shown to positively impact system performance, incorporating them into a MIMO system can increase the complexity and overall computational cost of channel estimation (CE). Despite the paramount pertinence of CE to RIS-aided communications, several studies have already addressed CE schemes for conventional RIS-aided environments, such as [32]–[37]. Therefore, we focus on designing a joint hybrid precoding and multiple RIS optimization framework and performing a system-level assessment under the assumption that full channel state information (CSI) was acquired beforehand.

The high attenuation present in the THz band is addressed by the implementation of UM-MIMO and its hybrid precoder framework. Instead of using fully digital precoders, it has become more important to adopt hybrid (digital-analog) architectures, as these require a reduced number of dedicated radio frequency (RF) chains, thus reducing the overall precoding complexity and consuming less power than fully digital solutions [38]. The implementation and benefits of hybrid precoding architectures have already been addressed and demonstrated in [18], [19], [21]–[23], [26], [29], [30], [39]–[45]. Although hybrid architectures were initially proposed to enhance energy efficiency by providing a lower RF-chain count than fully-digital architectures, works such as [18], [19], [21]–[23], [26], [29], [39] have demonstrated interest in applying hybrid precoding architectures to frameworks that aim to maximize the system's capacity due to their reduced implementation cost compared to fully-digital approaches. In addition, the authors in [39]–[41] have demonstrated that the analog precoding part can be reduced to a simple projection operation in a flexible precoding algorithm designed to cope with different precoding architectures. The authors in [29] present a beam training scheme with hierarchical codebooks and two cost-efficient hybrid beamforming designs for RIS-assisted massive MIMO. They propose a cooperative beam-training procedure in which the precoders, RIS matrices, and combiners are all optimized simultaneously. The authors in [30] propose a space-orthogonal scheme that jointly optimizes the precoders, RIS matrices, and decoders in a multi-user MIMO system. Both of the aforementioned works are highly relevant. However, the authors propose solutions that optimize multiuser transmission and detection and seek spatial orthogonalization. On the other hand, our work focuses on optimizing single-user MIMO links with multiple access established in time and frequency domains, whilst seeking a simple, low-complexity approach. Table 1 summarizes the most relevant works from the literature and compares them against the proposed framework.

This paper focuses on the design of an efficient and effective RIS-assisted wireless communication environment by optimizing the individual RIS elements and transceivers, in order to combat the severe distance limitation in the THz band. It is assumed that the system operates with orthogonal frequency division multiplexing (OFDM) and that multiple parallel RIS panels are deployed between the transmitter and receiver. The main goals of our study will be centered on the use of large antenna arrays at the transmitter and receiver, the implementation of hybrid schemes at the transmitter to reduce its complexity, and the implementation of an algorithm for optimal design of the precoder and RISs phase shifts. Physical layer simulations will be conducted to demonstrate the effectiveness of the proposed approach. In addition, the effect of the presence of multiple RIS panels on the system's aggregated throughput and coverage will also be addressed. The main contributions of this paper can be summarized as follows:

- We propose a joint hybrid precoder and multiple RIS optimization algorithm that maximizes the achievable rate of THz UM-MIMO communications. This algorithm also facilitates implementation in hardware-constrained systems, which are typical at these frequency bands. The proposed approach accomplishes this by separating the digital and analog precoder computations and adopting different hybrid architectures: fully connected (FC), array-of-subarrays (AoSA), and dynamic array-of-subarrays (DAoSA). Additionally, the algorithm can incorporate alternative implementations to phase shifters, such as switches and antenna selectors, for the analog component.

- To cope with the frequency-selective channels typical of THz UM-MIMO systems, the proposed algorithm considers multicarrier transmission. It assumes the adoption of multiple, parallel RIS panels deployed in the vicinity of the base station and users. This helps overcome the severe distance limitations of these bands.

- Link-level simulations demonstrate the efficiency and versatility of the algorithm. The results show that the algorithm enables different trade-offs between performance and implementation complexity compared to a fully digital refer-

TABLE 1. Comparison of supported configurations of the proposed algorithm with those of the relevant literature.

Reference	Optimization objective	Link	Hybrid Precoding	Multi-RIS	Multi-carrier	System-Level Assessment
[18]	Ergodic Sum-Rate	MISO	✓	✓	-	✓
[19]	Weighted Sum-Rate	MISO	✓	✓	✓	-
[20]	Transmit Power	MISO	-	-	-	✓
[21]	Achievable Rate	MIMO	✓	✓	-	-
[22]	Weighted Sum-Rate	MIMO	✓	-	✓	-
[23]	Achievable Sum-Rate	MISO	✓	✓	✓	-
[24]	Achievable Rate	MISO	-	-	✓	-
[25]	Outage Probability and Ergodic Capacity	MISO	-	-	-	-
[26]	Outage Probability and Achievable Rate	MIMO	✓	-	-	-
[29]	Achievable Sum-Rate	MIMO	✓	✓	-	-
[30]	Weighted Sum-Rate	MIMO	-	✓	-	-
Proposed	Achievable Rate	MIMO	✓	✓	✓	✓

ence approach. This makes the algorithm especially relevant in contexts where THz systems operate under severe hardware constraints.

- We present system-level simulations in which the proposed approach is integrated into a post-5G/6G radio access network (RAN) operating at 300 GHz. The evaluated environment corresponds to the 5G New Radio indoor office scenario. The results show that the maximum achievable throughput is obtained by distributing multiple parallel RIS panels throughout the environment. Adding multiple RIS panels to the office scenario reveals that the highest coverage and throughput gains occur with the lowest density settings, and the lowest gains occur with the highest density settings.

This paper is organized as follows: section II introduces the receive signal model and hybrid precoding architectures taken into account in the multicarrier RIS-assisted THz UM-MIMO system, section III presents the proposed hybrid precoding and RIS optimization algorithm. Section IV shows the numerical results and presents a description of the system model and the 5G New Radio (NR) scenario considered for the system-level assessment. Section V outlines the conclusions of our study.

Notation: Matrices and vectors are represented in boldface letters in uppercase and lowercase, respectively. The superscript $[.]^T$ and $[.]^H$ denote a transpose and conjugate transpose matrix/vector, respectively. $\mathbf{I}_{n\times n}$ is the identity matrix of dimension $n\times n$, $|.|$ is a modulus operator, $\|.\|_F$ is the Frobenius norm and $det(.)$ represents the determinant.

II. SYSTEM MODEL

Consider a UM-MIMO system operating in the THz band, characterized by an end-to-end channel matrix with N_{tx} transmit antenna arrays and N_{rx} receive antenna arrays. The communication link is established with the aid of N_{pan} RIS panels consisting of N_{ris} reflective elements. Fig. 1 illustrates the considered UM-MIMO system in an indoor environment with the direct channel between the BS and the user partially blocked by several existing obstacles.

The channel will be modeled assuming that the system adopts OFDM to cope with frequency-selective fading. Previous studies, such as [46]–[54], have already addressed the issue of frequency selectivity in systems operating in the

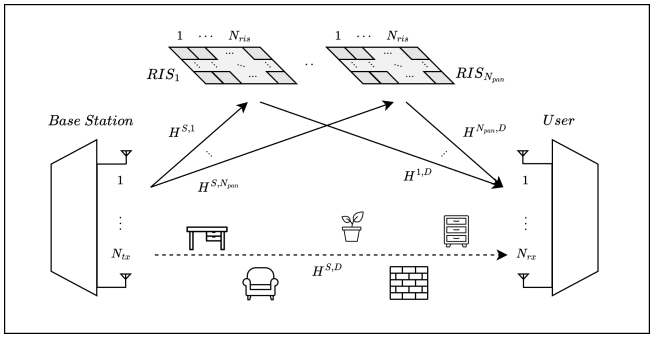

FIGURE 1. System model layout considered for the RIS-assisted UM-MIMO communication system.

mmWave/THz bands in indoor environments. Additionally, the work in [49], [51]–[54] included measurements of the indoor channel and demonstrated that, while the number of resolvable multipath components is small in the THz bands and thus less challenging than rich-scattering microwave channels, the used bandwidths tend to be greater than the coherence bandwidth, even in indoor environments. Additionally, although our evaluation was carried out in an office/indoor scenario, our approach can be applied to other environments, such as outdoors, where the 'frequency-selective' characteristic tends to be more pronounced. On the user end, after combining, the resulting vector, $\mathbf{r}_k^D$, for each subcarrier k of the modeled scenario can be represented as

$$\mathbf{r}_k^D = \sqrt{\rho}\mathbf{W}_k^H\mathbf{H}_k\mathbf{F}_{RF}\mathbf{F}_{BB_k}\mathbf{s}_k + \mathbf{W}_k^H\mathbf{n}_k \tag{1}$$

where $k = 1,\ldots,N_c$, N_c being the total number of subcarriers allocated to the user, the matrix $\mathbf{H}_k \in \mathbb{C}^{N_{rx}\times N_{tx}}$ represents the overall frequency domain channel matrix between each transmit and receive antenna, $\mathbf{s}_k \in \mathbb{C}^{N_s\times 1}$, is the symbol vector containing the amplitude and phase modulated symbols with $\mathbb{E}\{\|\mathbf{s}_k\|_2^2\} = N_s$, where N_s is the number of streams transmitted simultaneously. $\mathbf{F}_{BB_k} \in \mathbb{C}^{N_{RF}\times N_s}$ and $\mathbf{F}_{RF} \in \mathbb{C}^{N_{tx}\times N_{RF}}$ are the digital baseband and analog precoder matrices, respectively, assuming a total of N_{RF} RF chains, with $N_s \le N_{RF} \le N_{tx}$. $\mathbf{W}_k \in \mathbb{C}^{N_s\times N_{rx}}$ denotes the combiner matrix applied at the user, and ρ the power per stream and per subcarrier. The Gaussian noise vector, $\mathbf{n}_k \in \mathbb{C}^{N_{rx}\times 1}$, represents the N_{rx} complex noise components at the receiver,

assumed to be independent zero-mean circularly symmetric Gaussian samples with covariance $\sigma_n^2 \mathbf{I}_{N_{rx}}$ [55], [56].

Considering the MIMO system aided by N_{pan} parallel RIS panels, the overall channel matrix , $\mathbf{H}_k$, can be defined for each subcarrier k as

$$\mathbf{H}_k = \mathbf{H}_k^{S,D} + \sum_{i=0}^{Npan} \mathbf{H}_k{}^{i,D} \mathbf{\Phi}_i \mathbf{H}_k^{S,i} \tag{2}$$

where $\mathbf{H}_k^{S,D} \in \mathbb{C}^{N_{rx} \times N_{tx}}$ represents the direct channel between the BS and the user, $\mathbf{H}_k^{i,D} \in \mathbb{C}^{N_{rx} \times N_{ris}}$ the channel effect between the ith RIS and the user, $\mathbf{H}_k^{S,i} \in \mathbb{C}^{N_{ris} \times N_{tx}}$ the channel effect between the BS and the ith RIS and $\mathbf{\Phi}_i \in \mathbb{C}^{N_{ris} \times N_{ris}}$ is the ith RIS diagonal phase shift matrix, $\mathbf{\Phi}_i = diag(\boldsymbol{\varphi}_i)$ with $\boldsymbol{\varphi}_i = [\varphi_{i,1}, \ldots, \varphi_{i,N_{ris}}]^T$.

The RISs are modeled such that each element, $\varphi_{i,n} (i = 1, \ldots, N_{pan})(n = 1, \ldots, N_{ris})$, acts as a new signal source, capturing and redirecting the incoming signals transmitted by the BS. Assuming discrete phase shifts with N_b quantization bits, each $\varphi_{i,n}$ can take $M = 2^{N_b}$ possible phase shift values.

The considered THz model includes channels with a LoS and N_{ray} non-line-of-sight (NLoS) components, where the rays arrive in clusters [57]. If the distance between the BS and the RIS, $d_{S,i}$, is greater than the Fraunhofer distance defined as $D_F \triangleq 2L_{array}^2/\lambda$ [58], L_{array} being the largest dimension of the array, we can assume a far-field propagation model with planar wavefronts. Assuming one single ray per cluster and N_{ray} as the sum of all rays from all clusters, we can write the channel frequency response between the BS and the user, at subcarrier k, according to [59], as

$$\begin{aligned}\mathbf{H}_k^{S,D} = & \sqrt{\beta_{LOS}^{S,D}} e^{-j2\pi \frac{d_{S,D}}{\lambda_k}} \mathbf{a}_D(\phi_0^{D\leftarrow S}, \theta_0^{D\leftarrow S}) \mathbf{a}_S^H(\phi_0^{S\rightarrow D}, \theta_0^{S\rightarrow D}) \\ & + \sqrt{\frac{\beta_{NLOS}^{S,D}}{K_{Rice}}} \sum_{l=1}^{N_{ray}} \alpha_l^{S,D} \mathbf{a}_D(\phi_l^{D\leftarrow S}, \theta_l^{D\leftarrow S}) \\ & \times \mathbf{a}_S^H(\phi_l^{S\rightarrow D}, \theta_l^{S\rightarrow D}) e^{-j2\pi\tau_l f_k}\end{aligned} \tag{3}$$

which describes $\mathbf{H}_k^{S,D}$ as the sum of its LoS and NLoS components. It is also important to note that, in the adopted wideband channel model, the channel is considered to be flat for each subcarrier.

The subcarrier frequency, f_k, can be computed through $f_k = f_c + \frac{B}{N_c}(k - 1 - \frac{N_c - 1}{2})$, B being the bandwidth and f_c the carrier frequency. τ_l represents the delay of the lth path and K_{Rice} denotes the ratio between the LoS and NLoS components, indicating the quality of the channel and the relative fading the path is subjected to [60]. $\alpha_l^{S,D} \in \mathbb{C}^{N_{ray} \times 1}$ is the lth NLoS complex gain between the BS and the user, whereas $\beta_{LOS}^{S,D}$ and $\beta_{NLOS}^{S,D}$ represent the path loss of the LoS and NLoS channels, respectively.

An approximation of the path loss between the BS and the user can be calculated as [61]

$$\beta^{S,D} = \frac{G_{tx} G_{rx}}{(\frac{4\pi}{\lambda})^2 d_{S,D}^{\eta}} e^{k_{abs}(f) d_{S,D}} \tag{4}$$

where G_{tx} is the transmit antenna gain, G_{rx} the receive antenna gain, η is the path loss exponent, and $k_{abs}(f)$ is the coefficient of molecular absorption at frequency f [62].

The clusters and the rays within each cluster are modeled to have specific angles of arrival (AoAs) and departure (AoDs), so $\mathbf{a}_S(\phi_l^{S\rightarrow D}, \theta_l^{S\rightarrow D})$ and $\mathbf{a}_D(\phi_l^{D\leftarrow S}, \theta_l^{D\leftarrow S})$ represent the array response vectors at the AoD and AoA from the large transmitter antenna array at the BS to the receiver antenna array, respectively, for the considered azimuth ϕ_l and elevation θ_l.

Assuming a uniform planar array (UPA) implementation, the array response vectors for the transmitter and receiver can be calculated as [15], [63]

$$\begin{aligned}&\mathbf{a}_S(\phi_l^{S\rightarrow D}, \theta_l^{S\rightarrow D}) = \\ &\left[1, \ldots, e^{j\frac{2\pi}{\lambda} d_{tx}(p \sin\phi_l^{S\rightarrow D} \sin\theta_l^{S\rightarrow D} + q\cos\theta_l^{S\rightarrow D})}, \ldots\right]^T\end{aligned} \tag{5}$$

and

$$\begin{aligned}&\mathbf{a}_D(\phi_l^{D\leftarrow S}, \theta_l^{D\leftarrow S}) = \\ &\left[1, \ldots, e^{j\frac{2\pi}{\lambda} d_{rx}(p' \sin\phi_l^{D\leftarrow S} \sin\theta_l^{D\leftarrow S} + q'\cos\theta_l^{D\leftarrow S})}, \ldots\right]^T,\end{aligned} \tag{6}$$

respectively, with $p, q = 0, \ldots, \sqrt{N_{tx}} - 1$ and $p', q' = 0, \ldots, \sqrt{N_{rx}} - 1$, representing the relative position of the (p, q)th transmit antenna and (p', q')th receive antenna. d_{tx} and d_{rx} are the spacing between antennas composing the transmitter and receiver square array, respectively.

The channel frequency response at subcarrier k, between the BS and the ith RIS, $\mathbf{H}_k^{S,i}$, and between the ith RIS and the user, $\mathbf{H}_k^{i,D}$, can both be written in a similar way to (3), by replacing the AoDs and AoAs. The pathloss coefficients should also consider the distances between each pair and the gain of the RIS's elements. The array response vectors at the AoD and AoA from the large transmitter antenna array at the BS to the surface of the ith RIS, and from the surface of the ith RIS to the user, can also be calculated, similar to (5) and (6).

In specific cases where the distances $d_{S,D}$ (BS-User), d_{S,R_i} (BS-RIS i), or $d_{R_i,D}$ (RIS i-User) are less than the Fraunhofer distance, a spherical wavefront near-field (NF) propagation model should be assumed and (3) must be adapted, to include the effect of all the individual path distances between each transmitting-receiving antenna pair [64]. Therefore, assuming an NF propagation model and unit-normalized power radiation patterns along the directions of interest for both the transmitting and receiving antennas, we can rewrite (3), for subcarrier k, as [65]

$$\begin{aligned}\mathbf{H}_k^{S,D}(n, m) = & \sqrt{\beta_{LOS}^{m,n}} e^{-j2\pi \frac{d_{m,n}}{\lambda_k}} \\ & + \frac{1}{\sqrt{K_{Rice}}} \sum_{l=1}^{N_{ray}} \sqrt{\beta_{NLOS}^{m,n}(l)} |\alpha_l^{m,n}| e^{-j2\pi\tau_l^{m,n} f_k},\end{aligned} \tag{7}$$

thus, representing the channel frequency response between the m^{th} transmit antenna at the BS to the n^{th} receive antenna at the user. $\tau_l^{m,n}$ is the delay of the l^{th} path between elements m and n, and $\alpha_l^{m,n}$ is the complex gain of the l^{th} path between

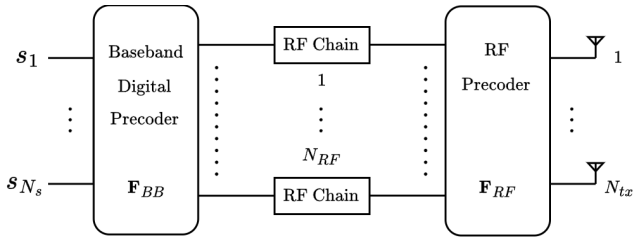

FIGURE 2. Hybrid precoder general model layout.

elements m and n normalized as $\sum_{l=1}^{N_{ray}} E[|\alpha_l^{m,n}|^2] = 1$. To compute the path loss of the LOS and NLOS channels, $\beta_{LOS}^{m,n}$ and $\beta_{NLOS}^{m,n}$, respectively, we consider the gains of the m^{th} transmit antenna at the BS and the n^{th} receive antenna at the user, and the distance of the individual (m,n) pair, $d_{m,n}$. For the NF model, the path loss coefficient between the m^{th} transmit antenna and the n^{th} receive antenna can be computed as [61], [65]

$$\beta^{m,n} = \frac{G_m G_n}{(\frac{4\pi}{\lambda})^2 (d_{m,n})^{\eta}} e^{k_{abs}(f) d_{m,n}}. \tag{8}$$

III. PROPOSED HYBRID PRECODER ALGORITHM

In this section, the algorithm for joint optimization of the hybrid precoder and RIS matrices is introduced.

A. ALGORITHM DERIVATION

After introducing the received signal model in section II, this subsection presents the problem formulation that aims to maximize the achievable rate in a multistream, multicarrier, and multi-RIS UM-MIMO link. Assuming perfect channel knowledge, the achievable rate, in bits per second per Hertz (bits/s/Hz), for the target user is given by [66]

$$R = \frac{N_f}{(N_f + N_{CP})N_c} \sum_{k=1}^{N_c} \log_2 \Bigg[\det \Big(\mathbf{I}_{N_s} + \frac{\rho}{P_n} \mathbf{F}_{BB_k}^H \mathbf{F}_{RF}^H \mathbf{H}_k^H \mathbf{H}_k \mathbf{F}_{RF} \mathbf{F}_{BB_k} \Big) \Bigg] \tag{9}$$

where N_c is the number of subcarriers allocated to the destination user, from a total of N_f subcarriers, N_{CP} the cyclic prefix length, and P_n the noise power of each subband.

With the goal of maximizing (9), we can describe the optimization problem as

$$\min_{\mathbf{F}_{RF},\, \mathbf{F}_{BB},\, \boldsymbol{\varphi}} \quad f(\mathbf{F}_{RF}, \mathbf{F}_{BB_1}, \ldots, \mathbf{F}_{BB_{N_c}}, \varphi_1, \ldots, \varphi_{N_{pan}}) = - \sum_{k=1}^{N_c} \log_2 \Bigg[\det \Big(\mathbf{I}_{N_s} + \frac{\rho}{P_n} \mathbf{F}_{BB_k}^H \mathbf{F}_{RF}^H \mathbf{H}_k^H \mathbf{H}_k \mathbf{F}_{RF} \mathbf{F}_{BB_k} \Big) \Bigg] \tag{10a}$$

$$\text{s.t.} \quad \|\mathbf{F}_{RF} \mathbf{F}_{BB_k}\|_F^2 \leq N_s \tag{10b}$$

$$\mathbf{F}_{RF} \in \mathcal{M}_{N_{tx} \times N_{RF}} \tag{10c}$$

$$|\varphi_{i,n}| = b,\ i = 1, \ldots, N_{pan},\ n = 1, \ldots, N_{ris} \tag{10d}$$

where $\mathcal{M}_{N_{tx} \times N_{RF}}$ is the set of feasible analog precoding matrices, depending on the chosen RF architecture, and b and $\varphi_{i,n}$ represent the amplitude response and the phase shift of the nth element from the ith RIS panel.

Although the objective function contains the hybrid precoder matrix divided into its digital and analog components, $\mathbf{F}_{BB_k}$ and $\mathbf{F}_{RF}$, respectively, as shown in Fig. 2, in order to reformulate the problem into a more convenient form, we introduce an auxiliary variable, $\mathbf{F}_k = \mathbf{F}_{RF} \mathbf{F}_{BB_k}$ with $\mathbf{F}_k \in \mathbb{C}^{N_{tx} \times N_s}$, and simplify the objective function. Considering that, the problem can be rewritten as

$$\min_{\mathbf{F}_{RF},\, \mathbf{F}_{BB},\, \mathbf{F},\, \boldsymbol{\varphi}} \quad f(\mathbf{F}_1, \ldots, \mathbf{F}_{N_c}, \varphi_1, \ldots, \varphi_{N_{pan}}) = - \sum_{k=1}^{N_c} \log_2 \Bigg[\det \Big(\mathbf{I}_{N_s} + \frac{\rho}{P_n} \mathbf{F}_k^H \mathbf{H}_k^H \mathbf{H}_k \mathbf{F}_k \Big) \Bigg] \tag{11a}$$

$$\text{s.t.} \quad \mathbf{F}_k = \mathbf{F}_{RF} \mathbf{F}_{BB_k} \tag{11b}$$

$$\|\mathbf{F}_{RF} \mathbf{F}_{BB_k}\|_F^2 \leq N_s \tag{11c}$$

$$\mathbf{F}_{RF} \in \mathcal{M}_{N_{tx} \times N_{RF}} \tag{11d}$$

$$|\varphi_{i,n}| = b,\ i = 1, \ldots, N_{pan},\ n = 1, \ldots, N_{ris} \tag{11e}$$

To ease complexity, we first solve the problem over $\mathbf{F}_k$ and $\boldsymbol{\varphi}_i$ only, relaxing constraints (11b) and (11d). This makes the problem simpler to address, being equivalent to optimizing for a fully-digital precoder, $\mathbf{F}_k$. The resulting simplified problem can then be represented as

$$\min_{\mathbf{F},\, \boldsymbol{\varphi}} \quad f(\mathbf{F}_1, \ldots, \mathbf{F}_{N_c}, \varphi_1, \ldots, \varphi_{N_{pan}}) = - \sum_{k=1}^{N_c} \log_2 \Bigg[\det \Big(\mathbf{I}_{N_s} + \frac{\rho}{P_n} \mathbf{F}_k^H \mathbf{H}_k^H \mathbf{H}_k \mathbf{F}_k \Big) \Bigg] \tag{12a}$$

$$\text{s.t.} \quad \|\mathbf{F}_k\|_F^2 \leq N_s \tag{12b}$$

$$|\varphi_{i,n}| = b,\ i = 1, \ldots, N_{pan},\ n = 1, \ldots, N_{ris} \tag{12c}$$

To find a solution for this optimization problem, we use the accelerated proximal gradient method (APGM) [67]. To implement this method, we can use the indicator function, which is defined for a generic set $\mathcal{A}$, as $\mathcal{I}_{\mathcal{A}}(x)$, returning 0

if $x \in \mathcal{A}$ and $+\infty$ otherwise. Therefore, we can rewrite the problem as

$$\min_{\mathbf{F},\boldsymbol{\varphi}} \quad f(\mathbf{F}_1,\ldots,\mathbf{F}_{N_c},\boldsymbol{\varphi}_1,\ldots,\boldsymbol{\varphi}_{N_{pan}}) + \sum_{k=1}^{N_c}\mathcal{I}_{\mathcal{D}}(\mathbf{F}_k) + \sum_{i=1}^{N_{pan}}\mathcal{I}_{\mathcal{U}_{N_{ris}}}(\boldsymbol{\varphi}_i) \tag{13a}$$

where $\mathcal{I}_{\mathcal{D}}$ and $\mathcal{I}_{\mathcal{U}_{N_{ris}}}$ are the indicator functions for sets $\mathcal{D}$ and $\mathcal{U}$, respectively, which are defined as

$$\mathcal{D} = \{\mathbf{X} \in \mathbb{C}^{N_{tx}\times N_s} : \|\mathbf{X}\|_F^2 \leq N_s\}, \tag{14}$$

and

$$\mathcal{U}_{N_{ris}} = \{\mathbf{u} \in \mathbb{C}^{N_{ris}\times 1} : |u_n| = a, \quad n = 1,\ldots,N_{ris}\}. \tag{15}$$

The APGM method consists of applying a gradient step, relative to $\mathbf{F}_k$ and $\boldsymbol{\varphi}_i$, followed by a proximal mapping. The variables used in the following gradient step are a linear combination of the two previous steps. This linear combination uses a weighting parameter, often called the extrapolation parameter, which can be computed for the qth iteration as

$$\omega^{(q)} = \frac{q}{q+3}. \tag{16}$$

The implementation of APGM corresponds to lines 2 to 7 in algorithm 1, which runs for Q iterations.

To complete the algorithm, constraints (11b) and (11d) are reintroduced, replacing the equality constraint (11b) by an approximation problem. This results in the following formulation for the second stage of the algorithm:

$$\min_{\mathbf{F}_{RF},\mathbf{F}_{BB}} \quad \sum_{k=1}^{N_c}\|\mathbf{F}_k - \mathbf{F}_{RF}\mathbf{F}_{BB_k}\|_F^2 \tag{17a}$$

$$\text{s.t.} \quad |F_{RF_{p,m}}| = a,\ p = 1,\ldots,N_{tx},\ m = 1,\ldots,N_{RF} \tag{17b}$$

$$\|\mathbf{F}_{RF}\mathbf{F}_{BB_k}\|_F^2 \leq N_s,\ k = 1,\ldots,N_c. \tag{17c}$$

In this case, we solve the minimization problem using the alternating direction method of multipliers (ADMM), as described in [39], which was first used in RIS-aided MIMO system design in [68]. The resulting algorithm consists of two computational cycles, the first Q iterations optimizing the precoder matrices, $\mathbf{F}_k$, as fully digital precoder matrices, according to the relaxation of the constraints (11b) and (11d), and the second Q' iterations optimizing its digital and analog components, $\mathbf{F}_{BB_k}$ and $\mathbf{F}_{RF}$, respectively. The resulting algorithm is summarized in algorithm 1, where $\propto$ represents the step size for each iteration of the APGM and $\mathbf{P}_k^{(\cdot)}$, $\mathbf{Y}_i^{(\cdot)}$, $\mathbf{R}^{(\cdot)}$ and $\mathbf{G}^{(\cdot)}$ are auxiliary variables used to compute the projection and apply the iterative evolution of the optimization variables.

The gradients can be found using the approach described in [69], resulting

$$\nabla_{\mathbf{F}_k^*} f(\mathbf{F}_k,\mathbf{Y}_i) = -\frac{\rho}{P_n}\mathbf{H}_k^H\mathbf{H}_k\mathbf{F}_k \times \left(\mathbf{I}_{N_s} + \frac{\rho}{P_n}\mathbf{F}_k^H\mathbf{H}_k^H\mathbf{H}_k\mathbf{F}_k\right)^{-1}, \tag{18}$$

and

$$\nabla_{\boldsymbol{\varphi}_i^*} f(\mathbf{F},\mathbf{Y}_i) = -\frac{\rho}{P_n}\sum_{k=1}^{N_c} diag\left[(\mathbf{H}_k^{i,D})^H\mathbf{H}_k\mathbf{F}_k \times \left(\mathbf{I}_{N_s} + \frac{\rho}{P_n}\mathbf{F}_k^H\mathbf{H}_k^H\mathbf{H}_k\mathbf{F}_k\right)^{-1}\mathbf{F}_k^H(\mathbf{H}_k^{S,i})^H\right]. \tag{19}$$

The total channel matrix, $\mathbf{H}_k$, varies with the RIS response vector, $\boldsymbol{\varphi}_i$, (or its extrapolated vector, $\mathbf{Y}_i$), which means that $\mathbf{H}_k$ will also be updated during algorithm iterations.

The function $prox_{\propto g}$ represents the proximal mapping applied to the APGM. In this case, g corresponds to the indicator function ,$\mathcal{I}$, of a set, which reduces $prox_{\propto g}$ to a Euclidean projection described as

$$prox_{\propto\mathcal{I}_{\mathcal{D}}}(\mathbf{Z}) = \begin{cases} \mathbf{Z} & , \|\mathbf{Z}\|_F^2 \leq N_s \\ \frac{\sqrt{N_s}}{\|\mathbf{Z}\|_F}\mathbf{Z} & , \text{otherwise} \end{cases}, \tag{20}$$

and

$$prox_{\propto\mathcal{I}_{\mathcal{U}}}(\mathbf{u}) = a(\mathbf{u} \oslash |\mathbf{u}|). \tag{21}$$

In step 11 in algorithm 1, $\prod_{\mathcal{M}}(.)$ is the Euclidean projection onto set $\mathcal{M}$, which can be calculated according to the hybrid architecture to be used [41].

The complexity of the fully digital precoder matrix design is primarily influenced by the computation of its gradient (used in line 3 of algorithm 1), which has a complexity of $\mathcal{O}(N_{tx}^2N_{rx})$. This calculation should be performed for every subcarrier and therefore represents a complexity of $\mathcal{O}(N_cN_{tx}^2N_{rx})$. The complexity of the RIS matrix design is primarily influenced by the computation of its gradient (used in line 4 of algorithm 1), which has a complexity of $\mathcal{O}(N_cN_{ris}N_{tx}N_{rx})$. This operation should be performed for each RIS panel and therefore represents a complexity of $\mathcal{O}(N_{pan}N_cN_{ris}N_{tx}N_{rx})$. As described in [39], the update of variables $\mathbf{F}_{RF}$ and $\mathbf{F}_{BB}$ (lines 9 and 10 of algorithm 1, respectively) represent a complexity order of $\mathcal{O}(N_sN_{RF}N_{tx} + N_{RF}^2N_{tx} + N_{RF}^3)$. The updates of the auxiliary variables $\mathbf{R}$ and $\mathbf{G}$ (lines 11 and 12 of algorithm 1, respectively) require simple element-wise sums and divisions, both representing a complexity of $\mathcal{O}(N_{RF}N_{tx})$. Therefore, for a total of Q and Q' iterations of the first and second stage of the proposed algorithm, respectively, and considering only the dominant terms, the overall complexity order for the proposed algorithm is $\mathcal{O}(Q(N_cN_{tx}^2N_{rx}+N_{pan}N_cN_{ris}N_{tx}N_{rx})+Q'(N_sN_{RF}N_{tx}+N_{RF}^2N_{tx}))$. This means that, in terms of complexity order, there is a quadratic dependency on the number of transmit antennas and RF chains considered in the hybrid architecture. Furthermore, the complexity of the APGM-ADMM algorithm grows linearly with the number of subcarriers, receive antennas, RIS elements and panels, and transmitted symbols.

B. HYBRID ARCHITECTURES

In this work, we employ various architectures of the analog precoder, as illustrated in Fig. 3, including fully connected (FC), array-of-subarrays (AoSA), and dynamic array-of-subarrays (DAoSA). Some variants of these architectures

Algorithm 1 APGM-ADMM Iterative optimization of the hybrid precoder and RIS matrices

Input: $\mathbf{r}_k^D, \mathbf{H}_k^{S,i}, \mathbf{H}_k^{i,D}, \mathbf{F}_k^{(0)}, \boldsymbol{\varphi}_i^{(0)}, \rho, \mathbf{Q}, \mathbf{Q}', \mathbf{R}^{(0)}, \mathbf{G}^{(0)}$
Output: $\hat{\mathbf{F}}_{BB}, \hat{\mathbf{F}}_{RF}, \boldsymbol{\varphi}_i^{(Q)}$

$\mathbf{P}_k^{(0)} \leftarrow \mathbf{F}_k^{(0)}, \mathbf{Y}_i^{(0)} \leftarrow \boldsymbol{\varphi}_i^{(0)}$
for $q = 0, ..., Q-1$ **do**
  $\mathbf{F}_k^{(q+1)} = prox_{\propto \mathcal{I}_{\mathcal{D}}}\left(\mathbf{P}_k^{(q)} - \propto \nabla_{\mathbf{F}_k^*} f(\mathbf{P}_k^{(q)}, \mathbf{Y}_i^{(q)})\right) \quad k = 1, ..., N_c$
  $\boldsymbol{\varphi}_i^{(q+1)} = prox_{\propto \mathcal{I}_{\mathcal{U}}}\left(\mathbf{Y}_i^{(q)} - \propto \nabla_{\mathbf{Y}_i^*} f(\mathbf{P}_k^{(q)}, \mathbf{Y}_i^{(q)})\right) \quad i = 1, ..., N_{pan}$
  $\mathbf{P}_k^{(q+1)} = \mathbf{F}_k^{(q+1)} + \frac{q}{q+3}\left(\mathbf{F}_k^{(q+1)} - \mathbf{F}_k^{(q)}\right) \quad k = 1, ..., N_c$
  $\mathbf{Y}_i^{(q+1)} = \boldsymbol{\varphi}_i^{(q+1)} + \frac{q}{q+3}\left(\boldsymbol{\varphi}_i^{(q+1)} - \boldsymbol{\varphi}_i^{(q)}\right) \quad i = 1, ..., N_{pan}$
end for
for $q' = 0, ..., Q'-1$ **do**
  $\mathbf{F}_{RF}^{(q'+1)} = \left(\sum_{k=1}^{N_c} \mathbf{F}_k^{(Q)} \mathbf{F}_{BB_k}^{(q')H} + \rho\left(\mathbf{R}^{(q')} - \mathbf{G}^{(q')}\right)\right)\left(\sum_{k=1}^{N_c} \mathbf{F}_{BB_k}^{(q')} \mathbf{F}_{BB_k}^{(q')H} + \rho \mathbf{I}_{N_{RF}}\right)^{-1}$
  $\mathbf{F}_{BB_k}^{(q'+1)} = \left(\mathbf{F}_{RF}^{(q'+1)H} \mathbf{F}_{RF}^{(q'+1)}\right)^{-1} \mathbf{F}_{RF}^{(q'+1)H} \mathbf{F}_k^{(Q)} \quad k = 1, ..., N_c$
  $\mathbf{R}^{(q'+1)} = \prod_{\mathcal{M}}(\mathbf{F}_{RF}^{(q'+1)} - \mathbf{G}^{(q')})$
  $\mathbf{G}^{(q'+1)} = \mathbf{G}^{(q')} + \mathbf{F}_{RF}^{(q'+1)} - \mathbf{R}^{(q'+1)}$
end for
$\hat{\mathbf{F}}_{RF} \leftarrow \mathbf{R}^{(Q')}$
$\hat{\mathbf{F}}_{BB} \leftarrow \left(\hat{\mathbf{F}}_{RF}^H \hat{\mathbf{F}}_{RF}\right)^{-1} \hat{\mathbf{F}}_{RF}^H \mathbf{F}_k^{(Q)}$
$\hat{\mathbf{F}}_{BB} \leftarrow \sqrt{N_s} \|\hat{\mathbf{F}}_{RF} \hat{\mathbf{F}}_{BB}\|_F^{-1} \hat{\mathbf{F}}_{BB}$

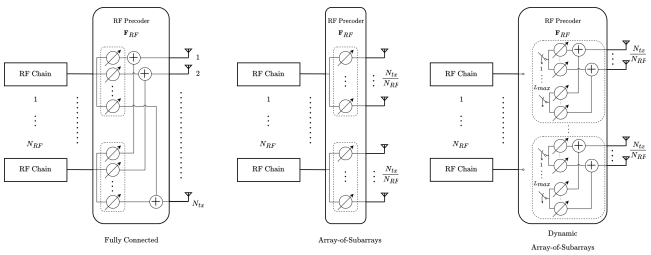

FIGURE 3. Fully connected (left), array-of-subarrays (middle), and dynamic array-of-subarrays (right) analog precoding architectures using phase-shifters and switches.

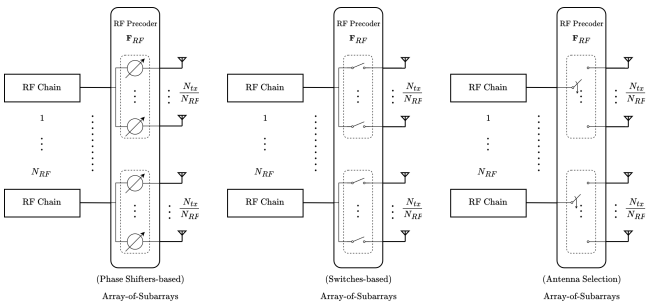

FIGURE 4. Phase shifters-based (left), switches-based (middle), and antenna selection (right) examples of the analog precoding architectures based on array-of-subarrays.

are also considered. As an example, Fig. 4 shows three variants of the AoSA architecture using phase shifters and switches. This subsection describes all of the architectures and variants that were considered in more detail.

1) Fully Connected (FC)

The FC hybrid design divides the signal coming from each RF chain into various phase shifters. Thereafter, the signal conveyed from each phase shifter from different RF chains is combined before its transmission in each antenna [17].

2) Array of Subarrays (AoSA)

The RF precoder that employs AoSA divides a group of antennas by the number of active RF chains, denominated as subarrays. In this work, the number of subarrays is set as N_{RF}, and the size of each subarray is given by N_{TX}/N_{SA}, thus dividing the number of transmitter antennas equally per each subset [41].

3) Dynamic Array of Subarrays (DAoSA)

In the AoSA design, each RF chain is connected directly to a fixed subset of antennas; in the DAoSA structure, however, each RF chain is linked to one or more subsets. Furthermore, it enables different numbers of subarrays to be connected to each RF chain, meaning different RF chains can have different numbers of transmit antennas [17], [70].

4) Unquantized Phase Shifters (UPS)

This architecture employs phase shifters with an infinite resolution. Can be used as a benchmark, since they can provide a closer performance to the fully digital RIS architecture, applying a phase between $[0, 2\pi[$.

5) Quantized Phase Shifters (QPS)

Although UPS structures can be seen as an ideal solution, QPS is a more realistic case since the number of phase shifts that can be implemented is finite. Assuming phase shifters with N_b bits, each one can take 2^{N_b} different values of phase.

6) Switches (Swi)

In this case, phase-shifters are replaced by switches, which will determine which antenna the signal will pass through.

7) Antenna Selection (AS)

In this architecture, the RF precoder will connect only one antenna per RF chain.

IV. NUMERICAL RESULTS

The results in this paper have been obtained using a Matlab simulator, based on the Monte Carlo method, to mimic a 6G indoor environment scenario in order to evaluate the performance of the algorithm that optimizes the hybrid precoder and the RISs, derived in section III, operating in the THz frequency band. Furthermore, the impact of the various hybrid architectures outlined in III-B, such as FC, AoSA, DAoSA, and their variations, will be analyzed and evaluated. As a benchmark, we refer to the fully digital framework presented in [65], which was extended to multi-carrier. In the scenario considered, the frequency is set to $f = 300$ GHz, and only the indirect path, transmitter-RIS-receiver, is active, with an obstructed LoS path, transmitter-receiver. The path loss exponent between the transmitter and RISs is equal to the path loss between RISs and the receiver, which is $n_{tx-ris} = n_{ris-rx} = 2.05$. The Rice factor is set to $K_{Rice} = 10$, and the bandwidth is $B = 8$ GHz. The distance between adjacent antenna elements in the transmitter, d_{tx}, in the RISs, d_{ris}, and in the receiver, d_{rx}, were assumed to be $d_{tx} = d_{rx} = d_{ris} = 5.4$ mm. Thus, the area of each RIS element is $A_{ris} = d_{ris}^2$. The coordinates of the BS, RIS, and user are defined as (0 m, 0 m), (2 m, 2 m), and (d_{tx-rx} m, 0 m), respectively, where d_{tx-rx} represents the distance between the transmitter and the receiver. Depending on the distance between each transmit and receive antenna pair, we apply either a far-field propagation model with planar wavefronts, or a near-field propagation model with spherical wavefronts, according to (3) or (7), respectively. The number of NLoS signal paths is set to 3, with $N_{rx} = 36$ receiver antennas, $N_{ris} = 1280$ elements, $N_s = 2$ streams, $N_{tx} = 2560$ transmit antennas, and $N_c = 115$ subcarriers.

A. LINK LEVEL RESULTS

The link-level evaluation results are presented in this subsection.

To evaluate the convergence behavior of the proposed approach, Fig. 5 presents the achievable rate (in bps/Hz) versus the iteration number, considering different fully and partially connected hybrid architectures. Each curve corresponds to a different hybrid architecture and shows how the proposed method converges at the end of the algorithm, after the optimized fully digital solution is disaggregated into its digital and analog components. Fig. 5 shows that our approach converges to a suboptimal solution in a relatively small number of algorithm iterations, regardless of the chosen hybrid architecture. Therefore, it has an overall low computational cost and low complexity.

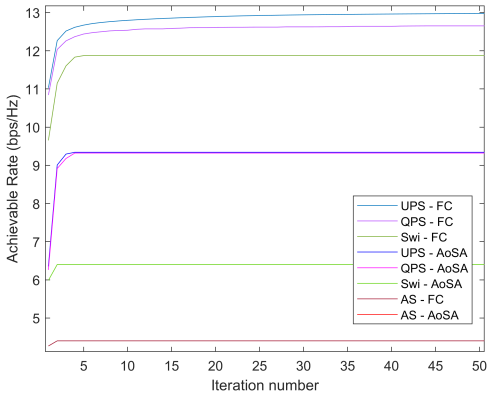

FIGURE 5. Achievable Rate convergence over iteration number of the proposed algorithm using different fully and partially connected precoding architectures. $N_{tx} = 2560$, $N_{rx} = 36$, $N_s = 2$, $N_{RF} = 8$, $N_c = 115$, $N_{ris} = 1280$, $N_{pan} = 1$, $P_{tx} = 37$ dBm, $d_{S,D} = 10$ m.

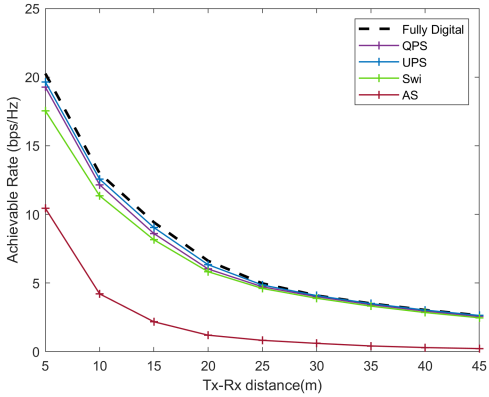

FIGURE 6. Achievable Rate vs Tx-Rx distance of the proposed algorithm for different fully connected precoding architectures. $N_{tx} = 2560$, $N_{rx} = 36$, $N_s = 2$, $N_{RF} = 8$, $N_c = 115$, $N_{ris} = 1280$, $N_{pan} = 1$, $P_{tx} = 37$ dBm.

Fig. 6 compares the achievable rate of different fully connected hybrid architectures, in bps/Hz, as the distance between the BS and the user increases, using the algorithm proposed in section III. Each curve corresponds to a different precoding architecture, and the parameters used are $N_{tx} = 2560$, $N_s = 2$, $N_{RF} = 8$, $N_{rx} = 36$ and the transmit power $P_{tx} = 5$W with $N_{ris} = 1280$ elements (for a single RIS panel). The worst performance is achieved using the AS architecture, which is expected since only one antenna is used per RF chain, which greatly reduces the degrees of freedom and consequently the achievable rate of the system. The fully connected structures using phase shifters and switches show much better results compared to the AS. The highest rates are achieved by the QPS and UPS architectures, which provide performances close to the fully digital precoder. As expected, UPS shows better results than the QPS architecture because it uses infinite resolution phase shifters.

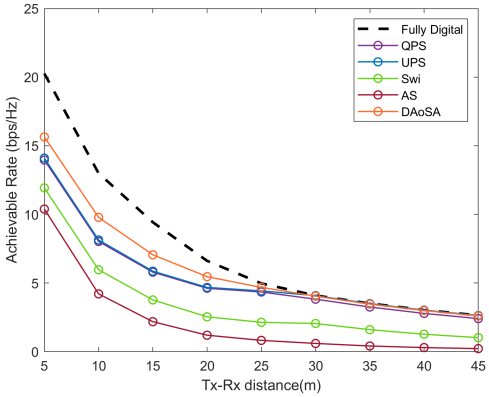

FIGURE 7. Achievable Rate vs Tx-Rx distance of the proposed algorithm for several variants of the AoSA hybrid precoding architecture. $N_{tx} = 2560$, $N_{rx} = 36$, $N_s = 2$, $N_{RF} = 8$, $N_c = 115$, $N_{ris} = 1280$, $N_{pan} = 1$, $P_{tx} = 37$ dBm.

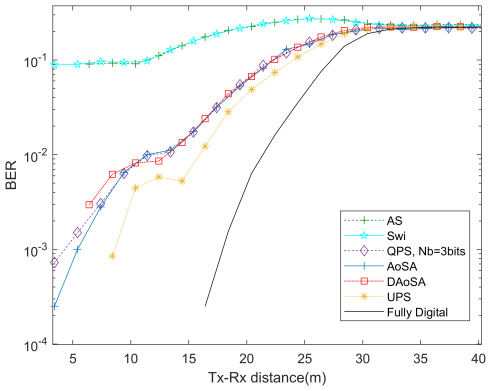

FIGURE 8. BER vs Tx-Rx distance of the proposed algorithm for several hybrid precoding architectures. $N_{t_x} = 2560$, $N_{r_x} = 36$, $N_s = 2$, $N_{RF} = 8$, $N_c = 1$, $N_{ris} = 1280$, $N_{pan} = 1$, $P_{tx} = 37$ dBm.

Fig. 7 compares the achievable rate of different AoSA hybrid architectures, in bps/Hz, as the distance between the BS and the user increases, using the algorithm proposed in section III. Each curve corresponds to a different precoding architecture, and the parameters used are $N_{tx} = 2560, N_s = 2$, $N_{RF} = 8$, $N_{rx} = 36$ and the transmit power $P_{tx} = 5$W with $N_{ris} = 1280$ elements (for a single RIS panel). For the same reasons, and similar to the performance of the fully connected AS architecture from Fig. 6, the worst performance is achieved when using the AS architecture. The DAoSA and the AoSA structures with phase shifters and switches show better results compared to the AS. The highest performance is achieved by the DAoSA architecture, with $L_{max} = 2$, which shows the curve closest to the fully digital precoder. As expected, the dynamic control of the circuit associated with the DAoSA architectures results in a higher spectral efficiency (SE), at the cost of more complexity than the AoSA architectures.

Fig. 8 shows the BER performance as a function of the distance between the BS and the user for several fully connected hybrid precoding architectures and for AoSA and DAoSA using quantized phase shifters. The parameters used are: $N_{tx} = 2560, N_s = 2, N_{RF} = 8, N_{rx} = 36$ and the transmit

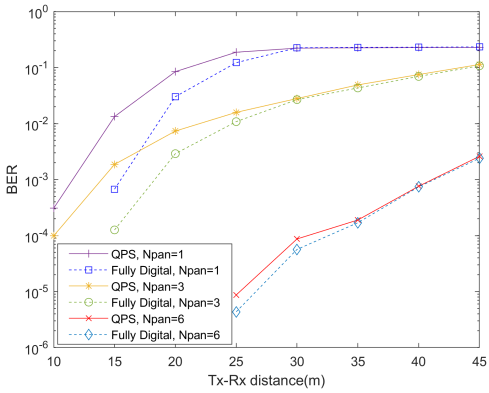

FIGURE 9. BER vs Tx-Rx distance of the proposed algorithm for the fully connected QPS hybrid precoding architecture, considering a variation in the number of RIS panels. $N_{tx} = 2560$, $N_{rx} = 36$, $N_s = 2$, $N_{RF} = 8$, $N_c = 115$, $N_{ris} = 1280$, $P_{tx} = 37$ dBm.

power $P_{tx} = 5$W with $N_{ris} = 1280$ elements (for a single RIS panel). The worst performance curves were obtained with the fully connected AS and Swi, where the BER did not reach values below 10^{-1}, even when the distance between the BS and the user is under 5 meters. The BER values obtained with AoSA, DAoSA, and fully connected UPS and QPS are quite similar, with the fully connected UPS reaching lower BER values compared to all other hybrid architectures when the distance between the BS and the user is less than 30 meters. Although there is still a gap to the fully-digital performance curve, this gap can be shortened by using a larger number of RIS panels, as shown in Fig. 9.

Fig. 9 shows the BER vs. distance for the fully connected QPS hybrid precoding architecture based on quantized phase shifters with a number of quantization bits, $N_b = 3$. Considering a variation in the number of RIS panels, the scenario parameters are $N_{tx} = 2560, N_s = 2, N_{RF} = 8, N_{rx} = 36$, and the transmit power $P_{tx} = 5$W with $N_{ris} = 1280$ elements per RIS panel. As expected, the smaller the distance, the lower the BER values for both architectures, and although the fully digital precoder achieves lower BER values, the behavior of the QPS is able to provide good performances and even approximate to fully digital in some conditions. In addition, it is clear that adding more RISs to the system improves the BER performance in both scenarios and reduces the differences in BER values between the hybrid and fully digital precoders.

B. SYSTEM LEVEL RESULTS

This subsection introduces the indoor office 5G New Radio scenario and assesses the performance of the proposed approach.

1) System-Level Model

In addition to link-level performance evaluations, system-level assessments are crucial for understanding the practical viability and scalability of multiple RIS-aided MIMO systems with hybrid precoding architectures. Link-level metrics

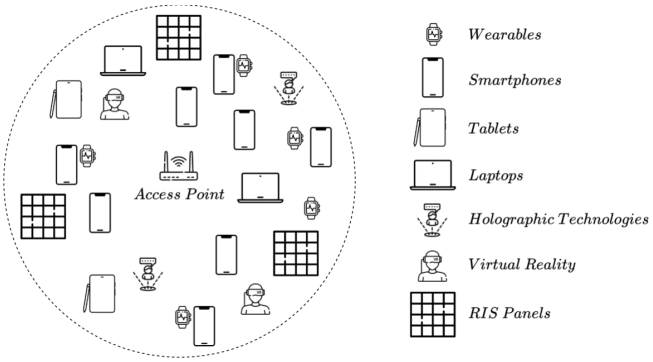

FIGURE 10. High-level diagram of a wireless network access point with RIS and user terminals.

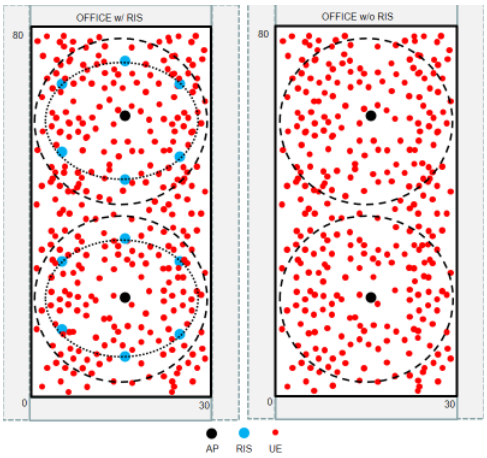

FIGURE 11. Illustration of the Indoor Office scenario with Access Points (AP) and UEs, with and without RIS.

TABLE 2. Simulation Parameters for the Office Scenario.

Parameter	Value
Carrier Frequency	300 GHz
Bandwidth	8 GHz
User Mobility	$0-3$ km/h
User distribution	Uniform
Maximum # subcarriers N_f	16560
Number of sectors	6
Transmit Power	37 dBm
Noise Figure	9 dB
Area of RIS elements	0.25 mm^2

offer insights into theoretical spectral efficiency and signal quality gains under ideal conditions, while system-level simulations capture broader network dynamics, such as user distribution, interference patterns, mobility, and resource allocation strategies. These evaluations offer a more holistic view of how the proposed methods perform in realistic deployment scenarios, highlighting potential bottlenecks and trade-offs that may be overlooked at the link level. Incorporating system-level results demonstrates the practical relevance of our approach by providing evidence of its effectiveness in large-scale networks and its potential to meet the performance demands of next-generation wireless systems.

The system-level evaluation assumes an indoor office scenario, which is the most appropriate given the range and path attenuation limitations of the THz band [71]. In this scenario, each user equipment (UE) receives data transmitted by the BS, also called an access point (AP), as illustrated in Fig. 10. A distinct property of the office scenario is the presence of furniture, which causes shadowing and much greater attenuation of the received power than the line-of-sight (LoS) path. This scenario involves the simultaneous use of two APs, which are assumed to cause AP-to-AP interference due to the high antenna gain used to compensate for high power attenuation over distance in THz bands.

In the considered scenario, there is a variable number of UEs, each at a height of 1.5 meters. The UEs are uniformly distributed within the available area. Due to the low probability of coverage in several areas inside the scenario, multiple RISs have been introduced. A set of 12 RISs extends coverage, increases the global throughput, and reduces the outage probability. The RISs are positioned on walls and ceilings around the APs, 10 meters away from each AP. The considered heights are 3 meters for ceiling-mounted antennas and RISs, and 2 meters for wall-mounted RISs. We built a 3D channel model for the aforementioned scenario in the THz frequency range based on the work in [72].

Fig. 11 illustrates the adopted network deployment. As can be seen in the figure, even with RISs, not all areas are completely covered. Specifically, areas far from the APs and RISs. In Fig. 11, the black dots represent the location of the APs, whose transmission range is outlined by black dotted lines; the blue dots represent the RISs, which are all located at the same distance from the corresponding AP (outlined by the black dotted line); and the red dots represent the UEs distributed throughout the office model area.

At 300 GHz, the transmission is characterized by significant signal attenuation, which limits the scenario coverage. To overcome this, we employ a large number of multi-antenna elements, namely 2560, to increase the transmit/receive capability of UM-MIMO through beamforming [73]. The path loss exponent is $n = 4.6$ for NLOS links between AP and users, and $n = 2.05$ for LOS links including the transmit antennas, the RIS and the receivers. The probability of having LOS and NLOS links depends on the distance, d, between the transmitter and receiver. The probability of LOS (P_{LOS}) can be written as

$$P_{LOS} = \begin{cases} 1 & , d \leq 1.2 \\ e^{-\frac{d-1.2}{4.7}} & , 1.2 \leq d \leq 6.5 \\ 0.32e^{-\frac{d-6.5}{32.6}} & , d \geq 6.5 \end{cases} \quad (22)$$

The parameters used in the simulations to characterize the office scenario are shown in table 2.

2) System-Level Performance

The system performance is evaluated in terms of coverage in percentages and throughput per sector in Gbps, considering two different configurations: AP/BS only and AP/BS with RISs distributed around the scenario. Each simulation curve

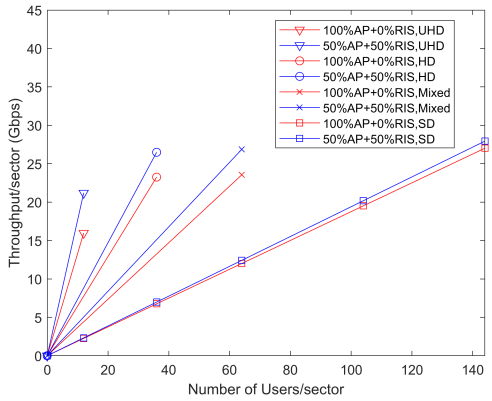

FIGURE 12. Throughput vs Number of users/sector of the proposed algorithm for different numbers of subcarriers per UE with and without RIS panels. $N_{tx} = 2560$, $N_{rx} = 36$, $N_{ris} = 1280$, $N_{pan} = 6$, $P_{tx} = 37$ dBm.

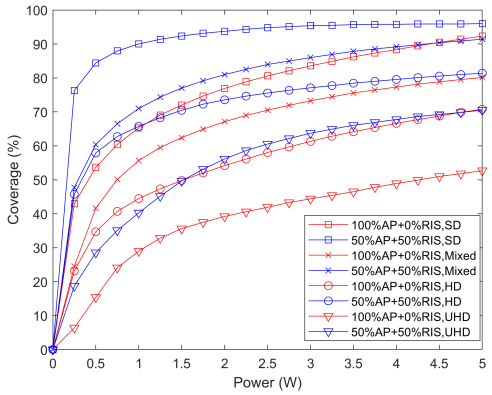

FIGURE 13. Coverage vs Power transmitted of the proposed algorithm for different numbers of subcarriers per UE with and without RIS panels. $N_{tx} = 2560$, $N_{rx} = 36$, $N_{ris} = 1280$, $N_{pan} = 6$, $P_{tx} = 37$ dBm.

has a label of the format $\%AP$+$\%RIS$. The curves consisting only of direct links between the AP/BS and the receivers are represented as $100\%AP$+$0\%RIS$, meaning that all UEs are connected to the AP/BS, while $50\%AP$+$50\%RIS$, means that 50% of the distributed UEs are connected to the nearest AP/BS and the remaining 50% are connected to the nearest RIS panels.

For the simulations, we considered three types of users. The first type is served by Ultra High Definition (UHD) video; the second, by High Definition (HD) video; and the third, by low-resolution Standard Definition (SD) video. These types are characterized by different signal-to-interference-plus-noise ratio (SINR) thresholds to ensure coverage of each received packet. UHD video requires receiving packets with 1380 subcarriers, resulting in a throughput of 2472.96 Mbps per user. For the HD video service, packets with 460 subcarriers are received, resulting in a throughput of 824.32 Mbps per user. For the SD video service, packets have 115 subcarriers, resulting in a throughput of 206.08 Mbps per user. An additional scenario consisting of a mixed video service with equal probabilities for UHD, HD, and SD video resolutions was evaluated. Specifically, one-third of the total subcarriers were allocated to UHD, one-third to HD, and one-third to SD. The average throughput is 1167.78 Mbps, corresponding to an average of 259 subcarriers. The required SINR for each video quality imposes strong limitations on the number of users that can be served. In order to facilitate beamforming for each RIS panel, given the large number of subcarriers, every panel was divided into subpanels of 1280 elements (arranged in $N_{col} = 40$ columns by $N_{row} = 32$ rows), each allocated to a different set of N_c subcarriers.

Fig. 12 shows the throughput per sector versus the number of users per sector. The constant parameters used are: $N_{tx} = 2560$, $N_s = 2$, $N_{rx} = 36$ and the transmit power $P_{tx} = 37$ dBm. The variable number of subcarriers that are characteristic of each curve is: $N_c = 1380$, $N_c = 460$, and $N_c = 115$ with $N_{ris} = 1280$ elements and $N_{pan} = 6$ RIS panels. Every curve involving the presence of RISs considers the proposed algorithm and fully digital precoding, assuming the existence of direct and indirect links between the transmitter and receivers. The number of UE receivers in the scenario for each simulation curve depends on the number of subcarriers per user. Based on the parameters of table 2, the maximum number of subcarriers within the bandwidth of 8 GHz is $N_c = 16560$. Curves with label "UHD" ($N_c = 1380$) have $N_u = 16560/1380 = 12$ users per sector, the curves with "HD" ($N_c = 460$) have $N_u = 16560/460 = 36$ users, and the "SD" ($N_c = 115$) include $N_u = 16560/115 = 144$ users in each sector. There are two curves with the label "Mixed", which consider 64 users per sector (4 UHD, 12 HD, and 48 SD video service users). The maximum throughput received by each user equipment, assuming transmission in one carrier with QPSK symbols, and two streams per subcarrier $N_s = 2$, depends on the number of subcarriers transmitted/received. We have considered in this scenario numerology 5 of 5G NR, where 14 OFDM symbols are transmitted every 31.25 µs. The spacing between subcarriers is 480 KHz. As observed from the performance curves, the introduction of RIS panels located at the same distance from the APs and spread around the scenario provides higher throughput compared to AP-only links. This is due to the reduction in the number of users experiencing outages. The throughput gain introduced by including RIS panels, compared to single AP links, depends on the video service quality and the number of users it serves. It increases as the number of users per sector decreases. The throughput relative gain for UHD video is 33% because the RISs can efficiently beamform for each user. For HD and mixed video, however, the gain drops to 14% due to the greater number of users served simultaneously. For SD video, the gain decreases to 3.4%, due to the large number of users that the set of included RIS panels cannot serve. This reduces the multiple access capacity of RIS beamforming for each user. However, increasing the number of users and decreasing video quality results in higher global throughput due to the small required SINR, despite main lobe degradation. As the number of users increases, more users will be close to the RIS panels, contributing to an increase in total throughput.

Fig. 13 shows coverage versus transmitted power for dif-

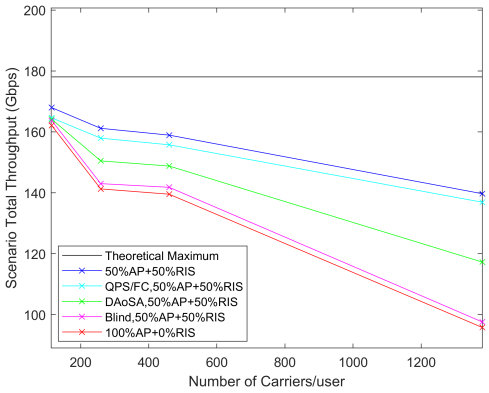

FIGURE 14. Aggregate Throughput vs Number of subcarriers per user of the proposed algorithm with and without RIS panels. $N_{tx} = 2560$, $N_{rx} = 36$, $N_{ris} = 1280$, $N_{pan} = 6$, $P_{tx} = 37$ dBm.

ferent video service types, each corresponding to a specific number of users per sector, under the same conditions as in Fig. 12. When we compare the coverage performance in Fig. 13 with the throughput performance in Fig. 12 at a maximum transmitted power of 5 W (37 dBm), we observe a direct correspondence between throughput and coverage. The curve "100%AP+0%RIS,UHD" achieves the smallest coverage of 53%. Adding RISs increases the coverage to 70.5% ("50%AP+50%RIS,UHD" curve), providing a maximum coverage gain of 33%. The coverage of the "100%AP+0%RIS,HD" curve is 71%. Compared to the "50%AP+50%RIS,HD" curve, which has a coverage of 81%, the coverage relative gain is 14%. A coverage gain of 14% is also observed between the two mixed service curves when RISs are included. The curve "100%AP+0%RIS,SD" achieves 90.5% coverage, compared to 95% coverage for the "50%AP+50%RIS,SD", giving a coverage gain of 5%. The coverage gains in Fig. 13 closely match the throughput gains in Fig. 12. Furthermore, only curve "50%AP+50%RIS,SD" achieves coverage above 90% with a transmitted power of 1 W. The other cases require a maximum power of 5 W to achieve maximum coverage. The highest coverage gain due to the introduction of RISs in the scenario occurs when the number of users per sector is reduced, and the number of subcarriers per user is increased. This case corresponds to the UHD video scenario, which achieves lower throughput and coverage performance globally. The SD video scenario achieves the highest throughput and coverage performance but, considering that it already shows good performances without RISs, it is the scenario presenting lower throughput and coverage gains when introducing RISs, specially when the transmitted power is high.

Fig. 14 illustrates the aggregate throughput for all office scenarios with a total of six sectors (see table 2) versus the number of subcarriers per user, considering a maximum transmit power of 37 dBm (5 W). We evaluate the global throughput for the same number of subcarriers per user as in the previous two figures, including the additional throughput for hybrid precoding architectures: fully connected QPS with 3-bit quantization (cyan, labeled as "QPS/FC") and DAoSA (green) with RIS in addition to APs. We also include a curve for blind RIS (magenta), which are reflective surfaces without reconfigurability capabilities and thus act as simple mirrors. For SD video quality ($N_c = 115$), there are 144 users per sector uniformly distributed inside the office. In terms of the number of users, this is the maximum load case. For HD video quality ($N_c = 460$), there are 36 users per sector, representing the intermediate load case. For UHD video quality ($Nc = 1380$), there is a total of 12 users per sector, which is the minimum load case in terms of number of users. For mixed video quality ($N_c = 259$), there are 64 users per sector. The red and blue curves correspond to the performance of the fully digital precoder, with only APs, and by deploying RISs in the vicinity of the APs, respectively. As shown in Fig. 14, the red curve indicates a minimum global throughput, irrespective of the scenario load, i.e., number of connected users, in comparison to the blue, cyan, green, and magenta curves. This observation aligns with the performance outcomes depicted in Fig. 12. As expected, the inclusion of RISs increases the global throughput independently of the scenario load. However, the highest throughput gain is achieved with the minimum load, and the lowest gain occurs with the maximum load. It is clear that the cyan curve with fully connected QPS shows minimal loss of throughput compared to the blue curve, which represents the fully digital system. The green curve with DAoSA shows a loss in throughput as the number of subcarriers per user increases, compared to the fully digital case, due to the high number of subcarriers and partial connections. As expected, the magenta curve with simple reflectors shows the least throughput gain compared to the AP-only scenario, regardless of the load. The reduced throughput gain from applying blind RISs to the system, compared to a system without RISs, emphasizes the importance of using reconfigurable RIS panels and a solution like the proposed algorithm to optimize system performance. The black curve represents the maximum theoretical throughput in this scenario. In this case, every transmitted packet is received without error. The curves of the maximum load case converge to this line but do not reach it. The minimum load case (UHD user) has the highest packet error rate, resulting in the lowest global throughput. The higher packet error rate in this case is due to the increased packet size and required SINR in the presence of multipath selective fading, as well as uncovered zones far from the APs and RISs.

V. CONCLUSION

In this paper, a RIS-based UM-MIMO scheme was investigated and studied with the aim of improving the communication system for THz frequencies to support 6G communication requirements. The system was designed to cope with several hybrid precoding architectures, which were evaluated to determine their capabilities to provide an achievable rate close to the one achieved by a fully digital precoder, while reducing the overall implementation complexity and energy costs. In addition, the performance of the system with and

without RIS was addressed in order to evaluate the impact of the addition of multiparallel RIS panels in the environment.

The link level results have shown that our system, when using hybrid beamforming structures, is capable of achieving SE levels close to the fully digital precoder scenario, while reducing the system's complexity and power requirements. Among the analog architectures assessed, the fully connected architecture using quantized and unquantized phase-shifters has shown the best performance in terms of achievable rate, as expected. Considering the AoSA architectures, the performances tend to be farther from the fully digital case, as also expected. Still, the version using dynamic switches for each RF chain, DAoSA, can achieve better rates than the other variants by trading off some additional implementation complexity.

System-level simulations for an office scenario using 300 GHz and with up to 216 RIS panels demonstrated the impact of the high absorption losses occurring at these frequencies, and showed the potential benefits of the deployment of a larger number of RIS elements and transmitter/receiver antennas to overcome the more severe distance limitation. The system-level results showed an overall increase in the system's throughput and coverage when several RIS panels are spread around the environment. We can conclude that the system's throughput and coverage gains, which come from the deployment of multiple RIS panels, depend hardly on the number and type of users with different video resolution services and the number of streams per user. Furthermore, results have shown that, independently of the scenario load, the system achieves higher throughput and higher coverage when the received signal at the UEs comes from both the APs and multiple RIS panels, instead of just the APs.

The work presented in this paper can be further extended by adapting the algorithm to cope with multiple users (multiuser) in the physical layer (link level), thus offering a centralized solution comprising a multiple number of streams (OFDM), users, and RIS panels for the UM-MIMO communication design.

REFERENCES

[1] I. F. Akyildiz, C. Han, and S. Nie, "Combating the distance problem in the millimeter wave and terahertz frequency bands," *IEEE Commun. Mag.*, vol. 56, no. 6, pp. 102–108, 2018.

[2] BR, "Recommendation ITU-R M.2083-0 IMT Vision-Framework and overall objectives of the future development of IMT for 2020 and beyond M Series Mobile, radiodetermination, amateur and related satellite services," http://www.itu.int/ITU-R/go/patents/en, Internation Telecommunication Union, Tech. Rep., 2015.

[3] S. R. Sabuj, M. Rubaiat, M. Iqbal, M. Mobashera, A. Malik, I. Ahmed, and M. A. Matin, "Machine-type communications in noma-based terahertz wireless networks," *Int. J. Intell. Netw.*, vol. 3, pp. 31–47, 2022.

[4] "The Next hyper Connected Experience for All," https://research.samsung.com/next-generation-communications#6gPop, Samsung, Tech. Rep., 12 2020.

[5] "Spectrum Expanding the Frontier 6G," "https://cdn.codeground.org/nsr/downloads/researchareas/2022May_6G_Spectrum.pdf", Samsung, Tech. Rep., 5 2022.

[6] S. M, "Machine learning and quantum computing for 5g/6g communication networks - a survey," *Int. J. Intell. Netw.*, vol. 3, pp. 197–203, 2022.

[7] S. Dash, C. Psomas, I. Krikidis, I. F. Akyildiz, and A. Pitsillides, "Active Control of THz Waves in Wireless Environments using Graphene-based RIS," *IEEE Trans. Antennas Propag.*, pp. 1–3, 2022.

[8] C. Han, Y. Wu, Z. Chen, and X. Wang, "Terahertz communications (teracom): Challenges and impact on 6g wireless systems," *arXiv preprint arXiv:1912.06040*, 2019.

[9] E. G. Larsson, O. Edfors, F. Tufvesson, and T. L. Marzetta, "Massive MIMO for next generation wireless systems," *IEEE Commun. Mag.*, vol. 52, pp. 186–195, 2014.

[10] R. Chataut and R. Akl, "Massive MIMO Systems for 5G and Beyond Networks—Overview, Recent Trends, Challenges, and Future Research Direction," *Sensors*, vol. 20, p. 2753, 05 2020.

[11] E. Björnson, Özdogan, and E. G. Larsson, "Reconfigurable intelligent surfaces: Three myths and two critical questions," *IEEE Commun. Mag.*, vol. 58, no. 12, pp. 90–96, 2020.

[12] S. Gong, X. Lu, D. T. Hoang, D. Niyato, L. Shu, D. I. Kim, and Y.-C. Liang, "Toward smart wireless communications via intelligent reflecting surfaces: A contemporary survey," *IEEE Commun. Surveys Tuts.*, vol. 22, no. 4, pp. 2283–2314, 2020.

[13] Q. Wu and R. Zhang, "Towards smart and reconfigurable environment: Intelligent reflecting surface aided wireless network," *IEEE Commun. Mag.*, vol. 58, no. 1, pp. 106–112, 2020.

[14] E. Basar and I. Yildirim, "Reconfigurable Intelligent Surfaces for Future Wireless Networks: A Channel Modeling Perspective," *IEEE Wireless Commun.*, vol. 28, no. 3, pp. 108–114, 2021.

[15] E. Basar, I. Yildirim, and F. Kilinc, "Indoor and Outdoor Physical Channel Modeling and Efficient Positioning for Reconfigurable Intelligent Surfaces in mmwave Bands," *IEEE Trans. Commun.*, vol. 69, no. 12, pp. 8600–8611, 2021.

[16] S. Dash, C. Psomas, I. Krikidis, I. F. Akyildiz, and A. Pitsillides, "Active control of thz waves in wireless environments using graphene-based ris," *IEEE Trans. Antennas Propag.*, vol. 70, no. 10, pp. 8785–8797, 2022.

[17] B. Ning, Z. Tian, W. Mei, Z. Chen, C. Han, S. Li, J. Yuan, and R. Zhang, "Beamforming technologies for ultra-massive mimo in terahertz communications," *IEEE Open J. Commun. Soc.*, vol. 4, pp. 614–658, 2023.

[18] C. Huang, Z. Yang, G. C. Alexandropoulos, K. Xiong, L. Wei, C. Yuen, Z. Zhang, and M. Debbah, "Multi-hop ris-empowered terahertz communications: A drl-based hybrid beamforming design," *IEEE J. Sel. Areas Commun.*, vol. 39, no. 6, pp. 1663–1677, 2021.

[19] X. Su, R. He, P. Zhang, and B. Ai, "Joint precoding for ris-assisted wideband thz cell-free massive mimo systems," *IEEE Internet Things J.*, vol. 11, no. 20, pp. 33 361–33 370, 2024.

[20] Y. Karacora, A. Umra, and A. Sezgin, "Robust communication design in ris-assisted thz channels," *IEEE Open J. Commun. Soc.*, vol. 6, pp. 3029–3043, 2025.

[21] I. Yildirim, A. Koc, E. Basar, and T. Le-Ngoc, "Multi-ris assisted hybrid beamforming design for terahertz massive mimo systems," *IEEE Open J. Commun. Soc.*, vol. 5, pp. 6150–6165, 2024.

[22] R. Amiri, "Peak downlink rate maximization and joint beamforming optimization for ris-aided thz ofdma um-mimo communications," *IEEE Wireless Commun. Lett.*, vol. 14, no. 2, pp. 375–379, 2025.

[23] W. Yan, W. Hao, C. Huang, G. Sun, O. Muta, H. Gacanin, and C. Yuen, "Beamforming analysis and design for wideband thz reconfigurable intelligent surface communications," *IEEE J. Sel. Areas Commun.*, vol. 41, no. 8, pp. 2306–2320, 2023.

[24] R. Su, L. Dai, and D. W. K. Ng, "Wideband precoding for ris-aided thz communications," *IEEE Trans. Commun.*, vol. 71, no. 6, pp. 3592–3604, 2023.

[25] H. Du, J. Zhang, K. Guan, D. Niyato, H. Jiao, Z. Wang, and T. Kürner, "Performance and optimization of reconfigurable intelligent surface aided thz communications," *IEEE Trans. Commun.*, vol. 70, no. 5, pp. 3575–3593, 2022.

[26] Y. Yang, S. Dang, M. Wen, B. Ai, and R. Qingyang Hu, "Blockage-aware robust beamforming in ris-aided mobile millimeter wave mimo systems," *IEEE Trans. Wireless Commun.*, vol. 23, no. 11, pp. 16 906–16 921, 2024.

[27] C. Cai, X. Yuan, and Y.-J. A. Zhang, "Ris partitioning based scalable beamforming design for large-scale mimo: Asymptotic analysis and optimization," 2023. [Online]. Available: https://arxiv.org/abs/2203.08377

[28] J. Wang, S. Gong, Q. Wu, and S. Ma, "Ris-aided mimo systems with hardware impairments: Robust beamforming design and analysis," *IEEE Trans. Wireless Commun.*, vol. 22, no. 10, p. 6914–6929, Oct. 2023. [Online]. Available: http://dx.doi.org/10.1109/TWC.2023.3246990

[29] B. Ning, Z. Chen, W. Chen, Y. Du, and J. Fang, "Terahertz multi-user massive mimo with intelligent reflecting surface: Beam training and hybrid

beamforming," *IEEE Trans. Veh. Technol.*, vol. 70, no. 2, pp. 1376–1393, 2021.
[30] B. Ning, P. Wang, L. Li, Z. Chen, and J. Fang, "Multi-irs-aided multi-user mimo in mmwave/thz communications: A space-orthogonal scheme," *IEEE Trans. Commun.*, vol. 70, no. 12, pp. 8138–8152, 2022.
[31] Y. Hou, G. Wang, C. Chen, G. Mu, Q. Cui, X. Tao, and Y. Yang, "220-ghz liquid crystal ris-aided multi-user terahertz communication system: Prototype design and over-the-air experimental trials," *IEEE Trans. Wireless Commun.*, vol. 25, pp. 8534–8545, 2026.
[32] Z.-Q. He and X. Yuan, "Cascaded channel estimation for large intelligent metasurface assisted massive mimo," *IEEE Wireless Commun. Lett.*, vol. 9, no. 2, pp. 210–214, 2019.
[33] J. He, H. Wymeersch, and M. Juntti, "Channel estimation for ris-aided mmwave mimo systems via atomic norm minimization," *IEEE Trans. Wireless Commun.*, vol. 20, no. 9, pp. 5786–5797, 2021.
[34] J. An, C. Xu, L. Gan, and L. Hanzo, "Low-complexity channel estimation and passive beamforming for ris-assisted mimo systems relying on discrete phase shifts," *IEEE Trans. Commun.*, vol. 70, no. 2, pp. 1245–1260, 2021.
[35] Y. Guo, P. Sun, Z. Yuan, C. Huang, Q. Guo, Z. Wang, and C. Yuen, "Efficient channel estimation for ris-aided mimo communications with unitary approximate message passing," *IEEE Trans. Wireless Commun.*, vol. 22, no. 2, pp. 1403–1416, 2023.
[36] M. Liu, X. Li, B. Ning, C. Huang, S. Sun, and C. Yuen, "Deep learning-based channel estimation for double-ris aided massive mimo system," *IEEE Wireless Commun. Lett.*, vol. 12, no. 1, pp. 70–74, 2023.
[37] P. Zheng, X. Lyu, Y. Wang, and Y. Gong, "Convolutional dictionary learning-based hybrid-field channel estimation for xl-ris-aided massive mimo systems," *IEEE Trans. Wireless Commun.*, vol. 24, no. 11, pp. 9085–9098, 2025.
[38] F. Sohrabi and W. Yu, "Hybrid digital and analog beamforming design for large-scale antenna arrays," *IEEE J. Sel. Topics Signal Process.*, vol. 10, no. 3, pp. 501–513, 2016.
[39] N. Souto, J. Silva, J. Pavia, and M. Ribeiro, "An alternating direction algorithm for hybrid precoding and combining in millimeter wave mimo systems," *Physical Communication*, vol. 34, pp. 165–173, 2019.
[40] J. P. Pavia, N. Souto, M. Ribeiro, J. Silva, and R. Dinis, "Hybrid precoding and combining algorithm for reduced complexity and power consumption architectures in mmwave communications," in *2020 IEEE 91st Vehicular Technology Conference (VTC2020-Spring)*, 2020, pp. 1–5.
[41] J. Pavia, V. Velez, R. Ferreira, N. Souto, M. Ribeiro, J. Silva, and R. Dinis, "Low complexity hybrid precoding designs for multiuser mmwave/thz ultra massive mimo systems," *Sensors*, vol. 21, p. 6054, 09 2021.
[42] K. Xu, Y. Cai, M. Zhao, Y. Niu, and L. Hanzo, "Mimo-aided nonlinear hybrid transceiver design for multiuser mmwave systems relying on tomlinson-harashima precoding," *IEEE Trans. Veh. Technol.*, vol. 70, no. 7, pp. 6943–6957, 2021.
[43] A. Vizziello, P. Savazzi, and K. R. Chowdhury, "A kalman based hybrid precoding for multi-user millimeter wave mimo systems," *IEEE Access*, vol. 6, pp. 55 712–55 722, 2018.
[44] D. H. N. Nguyen, L. B. Le, and T. Le-Ngoc, "Hybrid mmse precoding for mmwave multiuser mimo systems," in *2016 IEEE International Conference on Communications (ICC)*, 2016, pp. 1–6.
[45] L. Yan, C. Han, and J. Yuan, "A dynamic array-of-subarrays architecture and hybrid precoding algorithms for terahertz wireless communications," *IEEE J. Sel. Areas Commun.*, vol. 38, no. 9, pp. 2041–2056, 2020.
[46] J. Wang, C.-X. Wang, J. Huang, H. Wang, and X. Gao, "A general 3d space-time-frequency non-stationary thz channel model for 6g ultra-massive mimo wireless communication systems," *IEEE J. Sel. Areas Commun.*, vol. 39, no. 6, pp. 1576–1589, 2021.
[47] S. Kim and A. G. Zajić, "Statistical characterization of 300-ghz propagation on a desktop," *IEEE Trans. Veh. Technol.*, vol. 64, no. 8, pp. 3330–3338, 2015.
[48] S. Priebe, M. Jacob, and T. Kürner, "Angular and rms delay spread modeling in view of thz indoor communication systems," *Radio Sci.*, vol. 49, no. 3, pp. 242–251, 2014.
[49] Y. Xing, T. S. Rappaport, and A. Ghosh, "Millimeter wave and sub-thz indoor radio propagation channel measurements, models, and comparisons in an office environment," *IEEE Commun. Lett.*, vol. 25, no. 10, pp. 3151–3155, 2021.
[50] S. Ju, Y. Xing, O. Kanhere, and T. S. Rappaport, "Millimeter wave and sub-terahertz spatial statistical channel model for an indoor office building," *IEEE J. Sel. Areas Commun.*, vol. 39, no. 6, pp. 1561–1575, 2021.
[51] Y. Chen, Y. Li, C. Han, Z. Yu, and G. Wang, "Channel measurement and ray-tracing-statistical hybrid modeling for low-terahertz indoor communications," *IEEE Trans. Wireless Commun.*, vol. 20, no. 12, pp. 8163–8176, 2021.
[52] Y. Chen, C. Han, Z. Yu, and G. Wang, "Channel measurement, characterization, and modeling for terahertz indoor communications above 200 ghz," *IEEE Trans. Wireless Commun.*, vol. 23, no. 6, pp. 6518–6532, 2024.
[53] M. Kim, A. Ghosh, R. Takahashi, and K. Shibata, "Indoor channel measurement at 300 ghz and comparison of signal propagation with 60 ghz," *IEEE Access*, vol. 11, pp. 124 040–124 054, 2023.
[54] H. Zhao, L. Wei, M. Jarrahi, and G. J. Pottie, "Extending spatial and temporal characterization of indoor wireless channels from 350 to 650 ghz," *IEEE Trans. THz Sci. Technol.*, vol. 9, no. 3, pp. 243–252, 2019.
[55] J. Praia, J. Pavia, N. Souto, and M. Ribeiro, "Phase shift optimization algorithm for achievable rate maximization in reconfigurable intelligent surface-assisted thz communications," *Electronics*, vol. 11, p. 18, 12 2021.
[56] S. Jayaweera and H. Poor, "Capacity of multiple-antenna systems with both receiver and transmitter channel state information," *IEEE Trans. Inf. Theory*, vol. 49, no. 10, pp. 2697–2709, 2003.
[57] A. Saleh and R. Valenzuela, "A Statistical Model for Indoor Multipath Propagation," *IEEE J. Sel. Areas Commun.*, vol. 5, no. 2, pp. 128–137, 1987.
[58] F. Bohagen, P. Orten, and G. E. Oien, "On spherical vs. plane wave modeling of line-of-sight mimo channels," *IEEE Trans. Commun.*, vol. 57, no. 3, pp. 841–849, 2009.
[59] X. Yu, J.-C. Shen, J. Zhang, and K. B. Letaief, "Alternating minimization algorithms for hybrid precoding in millimeter wave mimo systems," *IEEE J. Sel. Topics Signal Process.*, vol. 10, no. 3, pp. 485–500, 2016.
[60] J. Ren and R. G. Vaughan, "Rice Factor Estimation from the Channel Phase," *IEEE Trans. Wireless Commun.*, vol. 11, no. 6, pp. 1976–1980, 2012.
[61] K. Dovelos, S. D. Assimonis, H. Quoc Ngo, B. Bellalta, and M. Matthaiou, "Intelligent reflecting surfaces at terahertz bands: Channel modeling and analysis," in *2021 IEEE International Conference on Communications Workshops (ICC Workshops)*, 2021, pp. 1–6.
[62] K. Dovelos, S. D. Assimonis, H. Q. Ngo, B. Bellalta, and M. Matthaiou, "Intelligent Reflecting Surfaces at Terahertz Bands: Channel Modeling and Analysis," *2021 IEEE Int. Conf. on Comm. Workshops, ICC Workshops 2021 - Proceedings*, 6 2021.
[63] O. E. Ayach, S. Rajagopal, S. Abu-Surra, Z. Pi, and R. W. Heath, "Spatially Sparse Precoding in Millimeter Wave MIMO Systems," *IEEE Trans. Wireless Commun.*, vol. 13, no. 3, pp. 1499–1513, 2014.
[64] J. Huang, C.-X. Wang, Y. Sun, R. Feng, J. Huang, B. Guo, Z. Zhong, and T. J. Cui, "Reconfigurable intelligent surfaces: Channel characterization and modeling," *Proc. IEEE*, vol. 110, no. 9, pp. 1290–1311, 2022.
[65] N. Souto and J. C. Silva, "Joint beamforming algorithm for multi-stream mimo systems assisted by multiple reconfigurable intelligent surfaces," *IEEE Open J. Commun. Soc.*, vol. 4, pp. 1317–1333, 2023.
[66] S. Zhang and R. Zhang, "Capacity characterization for intelligent reflecting surface aided mimo communication," *IEEE J. Sel. Areas Commun.*, vol. 38, no. 8, pp. 1823–1838, 2020.
[67] N. Parikh and S. Boyd, "Proximal algorithms," *Found. Trends Optim.*, vol. 1, no. 3, pp. 127–239, 2014.
[68] B. Ning, Z. Chen, W. Chen, and J. Fang, "Beamforming optimization for intelligent reflecting surface assisted mimo: A sum-path-gain maximization approach," *IEEE Wireless Commun. Lett.*, vol. 9, no. 7, pp. 1105–1109, 2020.
[69] A. Hjørungnes, *Complex-Valued Matrix Derivatives: With Applications in Signal Processing and Communications*. Cambridge University Press, 2011.
[70] L. Yan, C. Han, and J. Yuan, "A Dynamic Array-of-Subarrays Architecture and Hybrid Precoding Algorithms for Terahertz Wireless Communications," *IEEE J. Sel. Areas Commun.*, vol. 38, pp. 2041–2056, 9 2020.
[71] J. Pavia, V. Velez, N. Souto, M. Marques da Silva, and A. Correia, "System-level assessment of massive multiple-input–multiple-output and reconfigurable intelligent surfaces in centralized radio access network and iot scenarios in sub-6 ghz, mm-wave, and thz bands," *Applied Sciences*, vol. 14, 01 2024.
[72] Y. Xing, T. S. Rappaport, and A. Ghosh, "Millimeter wave and sub-thz indoor radio propagation channel measurements, models, and comparisons in an office environment," *IEEE Commun. Lett.*, vol. 25, no. 10, pp. 3151–3155, 2021.
[73] K. Rikkinen, P. Kyosti, M. E. Leinonen, M. Berg, and A. Parssinen, "Thz radio communication: Link budget analysis toward 6g," *IEEE Commun. Mag.*, vol. 58, no. 11, pp. 22–27, 2020.

DIOGO MENDES (Graduate Student Member, IEEE) received the Graduate and Master's degrees in Telecommunications and Computer Engineering from Iscte-Instituto Universitário de Lisboa (ISCTE), Lisbon, Portugal, in 2019. He is currently a Student Researcher with Instituto de Telecomunicações (IT), and ISCTE, Portugal, where he is currently working towards the Ph.D. degree in Information Science and Technology in the areas of wireless communications and signal processing for telecommunications. His research interests include physical layer algorithms for massive MIMO and reconfigurable intelligent surfaces, wireless transceivers, channel estimation, modulation and coding schemes, and signal processing for communications. He is a member of the IEEE Communications Society and Chair of the IEEE ISCTE Student Branch.

JOÃO PEDRO PAVIA (Member, IEEE) received his PhD in Information Sciences and Technologies in 2022 and he is currently an Assistant Professor in the Digital Technologies Department of the School of Applied Digital Technologies at ISCTE - University Institute of Lisbon, where he coordinates the Bachelor Degree in Digital Technologies and Information Security. He is a member of the IEEE and is also a member of COST - European Cooperation in Science and Technology, where he collaborates with professionals from various countries to develop solutions focused on the field of intelligent radio communications for seamless, inclusive interactions. In addition, another of his collaborations is related to the development of physical layer security solutions for reliable and resilient 6G systems. He has been involved as a local organizer and reviewer at several conferences and symposia. He is also a reviewer for several journals in the field of information sciences and technologies. His research interests include topics related to cybersecurity, wireless communication networks, artificial intelligence, and big data.

NUNO SOUTO (Senior Member, IEEE) received the Graduate degree in aerospace engineering-avionics branch from Instituto Superior Técnico, Lisbon, Portugal, in 2000, and the Ph.D. degree in 2006. From November 2000 to January 2002, he was a Researcher in automatic speech recognition with Instituto de Engenharia e Sistemas de Computadores, Lisbon. He joined the University Institute of Lisbon (ISCTE) as an Assistant Professor in 2006. He has been a Researcher with Instituto de Telecomunicações (IT), Portugal, since 2002, and has been involved in several international research projects and many national projects. His research interests include wireless networks, signal processing for communications, multicarrier communications, frequency domain equalization, channel coding, modulation, channel estimation, synchronization, MIMO schemes, wireless sensor networks, unmanned aerial vehicles, mmWave/terahertz communications, machine learning for wireless communications, and molecular communications. He is a member of the IEEE Communications Society.

JOÃO SILVA received the B.S. degree in aerospace engineering from the Instituto Superior Técnico, Lisbon Technical University, in 2000, and the M.B.A. degree from ISEG in 2015. From 2000 to 2002, he worked as a Business Consultant with McKinsey & Company. He finished his Ph.D. thesis with IST in 2006, focusing on spread spectrum techniques, multiuser detection schemes, and MIMO systems. Since 2006, he has been working on computer networks as an Assistant Professor with ISCTE-IUL.

AMÉRICO CORREIA (Senior Member, IEEE) received the B.Sc. degree in electrical engineering from the University of Angola, in 1983, and the M.Sc. and Ph.D. degrees in telecommunications from Instituto Superior Técnico (IST), Lisbon, Portugal, in 1990 and 1994, respectively. From 1991 to 1999, he was with IST as an Assistant Professor. From August 2000 to November 2007, he was an Associate Professor with ISCTE. Since December 2007, he has been a Full Professor with ISCTE, Lisbon University Institute, Portugal. He has been a Researcher with Instituto de Telecomunicações (IT), Portugal, since 1992. He was a Postgraduate Researcher with RWTH, Aachen, Germany, from October 1994 to September 1995. He visited the Nokia Research Center from September to December 1998 as a Visiting Scientist. From September 2000 to August 2001, he joined Ericsson Eurolab, the Netherlands. His research interests include CDMA, OFDMA, NOMA, MIMO, radio resource management, broadcasting technology, and enhanced multimedia broadcast/multicast services. He is a member of the Communications Society of IEEE and has been a member of "Ordem dos Engenheiros," since 1987.